ACS APPLIED ENERGY MATERIALS

Open Access
This article is licensed under CC-BY-NC-ND 4.0

www.acsaem.org
Article

Unveiling the Tunable Li Diffusion in MXenes Bilayers: Insights from First-Principles Study

Tanawat Sawasdee, Thanundon Kongnok, Ittipon Fongkaew, Suwit Suthirakun, Adisak Boonchun, Pakpoom Reunchan, Narasak Pandech, Jariyanee Prasongkit, and Sirichok Jungthawan*

Cite This: https://doi.org/10.1021/acsaem.4c01011
Read Online

ACCESS | Metrics & More | Article Recommendations | Supporting Information

ABSTRACT: The properties of 2D transition-metal carbides (MXenes) with the composition M_2CT_2 (where M = Sc, Ti, V, Nb, and Cr; and T = O and F) have been investigated. Employing first-principles calculations based on density functional theory, our study comprehensively explores the attributes of monolayer and bilayer MXenes. We focus on characteristics such as stability, diffusion, and selectivity of a lithium atom, along with cointercalation phenomena within Ti_2CO_2 bilayers. In the context of monolayers, we examine six distinct adsorption sites for functional atoms (T) on the surfaces of M_2CT_2. Energetically favorable monolayer configurations are identified for subsequent investigations involving bilayers. Structural modifications, including variations in layer types and stacking shifts, potentially alter the properties of the M_2CT_2 multilayer. The role of bilayer interfaces is crucial in understanding the insertion effects of Li atoms between layers as interlayer spacing can be dynamically adjusted through intercalation processes. We explore the structural relaxation of Ti_2CO_2 bilayers both with and without cointercalation. We analyze key lithium atom diffusion properties, such as diffusion barriers, diffusion rates, and relative diffusion rates (selectivity). Our findings reveal the tunability of the diffusion barrier in relation to interlayer spacing. By introducing specific cointercalated metals, such as potassium, the Li diffusion barrier can be dramatically reduced from 0.36 eV to approximately 0.01 eV. This reduction occurs as the interlayer spacing increases from 3.4 to 4.1 Å, enabling a Li atom to move nearly free between the Ti_2CO_2 layers. Notably, larger interlayer spacing gradually elevates the diffusion barrier toward the monolayer value as the Li atom prefers surface migration on either layer. Our work presents a comprehensive computational framework for understanding cointercalation in MXenes bilayers, shedding light on the intricate interplay between the structure and Li mobility.

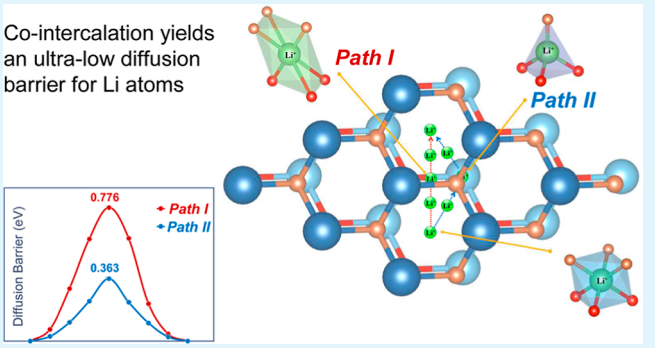

KEYWORDS: *MXenes, cointercalation, Li diffusion, K diffusion, lithium, potassium, bilayer, stacking stability*

Downloaded via 58.136.255.124 on July 19, 2024 at 14:35:22 (UTC).
See https://pubs.acs.org/sharingguidelines for options on how to legitimately share published articles.

1. INTRODUCTION

Energy storage materials are crucial to current technology, such as Li-ion batteries (LIBs) for transportation and energy storage devices. To date, extensive research has investigated and developed a satisfactory electrode material with good electrical conductivity, higher capacities, longer lifetimes, excellent cycling stability, and a higher charging rate than current materials. Primarily, graphene with a two-dimensional (2D) structure has remarkable electrochemical properties, such as large-surface areas, low migration barriers, and wide voltage windows. Graphene has been utilized as an electrode material for rechargeable LIBs.[1] Furthermore, other 2D materials, such as transition-metal dichalcogenides (TMDs)[2] and transition-metal carbides and nitrides (MXenes),[3−5] have been widely studied and shown to have high specific capacities and extremely high charging rates and have a high potential to be used as anode materials for LIBs.

The MXenes with multilayer structures are made by selectively etching specific atomic layers from their bulk precursors, e.g., Sc_2AlC and Ti_2AlC. MAX phases are denoted by $M_{n+1}AX_n$, where n = 1, 2, or 3, "M", "A", and "X" represent an early transition metal (e.g., Sc, Ti, Zr, Hf, V, Nb, Ta, Cr, and Mo), etched A element or A group (Al, Si, Ga, In, and Sn), and carbon (C) or nitrogen (N) (here we focused on X = C), respectively.[3,6−9] Chemical exfoliation, such as removing the "A" atom with aqueous hydrofluoric acid (HF) or by in situ formation of HF through the hydrochloric acid (HCl) and fluoride reaction, is the most widely used method to fabricate

Received: April 22, 2024
Revised: July 5, 2024
Accepted: July 7, 2024

© XXXX The Authors. Published by American Chemical Society

them.[10−12] MXenes are an extensive family of 2D materials with a chemical formula of $M_{n+1}X_n$, denoted as bare-MXenes. MXenes with functional groups denoted as $M_{n+1}C_nT_m$, where T_m represents the functional groups, such as the O, F, and OH atoms, that generally cover the surface of MXenes during the synthesis process. MXenes are among the most competitive 2D materials due to their varied chemical composition and customizable structure. As a result, an expanding family of MXenes has emerged as a key contender for a variety of applications, including electrode materials for energy storage devices such as alkali-metal ion (Li^+, K^+, and Na^+) batteries, supercapacitors, ion capacitors, hydrogen storage, and hydrogen harvesting material from photocatalytic processes.[13−21] The ultralarge interlayer spacing, e.g., 0.24−0.27 nm in Ti_2C-MXenes[22] and ∼0.9 nm in Ti_3C_2-MXenes,[23] makes MXenes easier to intercalate ions. It has attracted huge attention for high-performance capacitors.[15,23] The spontaneous intercalation of cations from aqueous salt solutions, such as Na^+, K^+, NH^{4+}, and Al^{3+}, has been demonstrated between the Ti_3C_2 multilayer and found that this variety of cations can be intercalated electrochemically, offering capacitances greater than 300 $F{\cdot}cm^{-3}$.[24] Increasing interlayer spacing and delamination for multilayers of MXenes is necessary to increase their adsorption capacities (approximately 410 $mA{\cdot}h{\cdot}g^{-1}$).[4]

Density functional theory (DFT) calculations are a powerful tool for understanding the properties of materials, which are important to further improving their performance. As a result, several methods from DFT calculations have been used to identify the promising properties of electrode materials for LIBs, i.e., gravimetric capacitance, Li mobility, and a desirable reaction from the voltage calculation. Changes in transition-metal species and surface functional groups can significantly affect the gravimetric capacity and cell voltage. In terms of theoretical gravimetric capacity for Li, Na, and Mg atoms, the reports reveal that the MXenes with low formula weights, e.g., Sc_2C, Ti_2C, V_2C, and Cr_2C, outperform their M_3C_2 and M_4C_3 counterparts.[20] Furthermore, it has been determined that M_2C compounds—both nonfunctionalized and O-functionalized—represent the most promising class of materials in terms of gravimetric capacity, which is greater than graphite (>400 $mA{\cdot}h{\cdot}g^{-1}$) and anode voltage, which is in the range of 0.2 to 1.0 V.[20]

The diffusion properties of Li atoms within a material are related to their mobility on the surface of the material, which is determined by the interactions between Li atoms and functional groups or surface atoms. By modification of the surface of the material, it is possible to alter the nature and strength of these interactions and thereby tune the diffusion properties of the Li atom to make it more suitable for specific applications. The Li mobility on the surface of M_2C MXenes, where M is Ti, V, Cr, Zr, Hf, Ta, and Mo, has been predicted to be significantly low compared to TMDs, e.g., MoS_2, and graphene.[25,26] However, the unavoidable formation of the functional groups, such as O, F, and OH, caused the Li atom diffusion barrier to reach around 10 times greater than that of the nonfunctional group structure.[26] Interestingly, applying the biaxial strain to the monolayers of Ti_2C, Ti_2CO_2, and Ti_2CF_2 leads to a greater Li atom diffusion barrier.[26] Although theoretical studies suggest that monolayer MXenes are superiorly anticipated to perform as LIBs in terms of diffusion ability and gravimetric capacity, they cannot directly compare them to practical multilayer compounds, which are essential for predicting the anode efficiency. For example, many systematic investigations of the Li capabilities for bilayer MXenes, such as V_2CO_2 and Ti_2CO_2, correlate more closely with experiment results than the prior calculations for the monolayer.[5,8,20,27] However, the diffusion barriers simulated using CI-NEB for $Ti_{n+1}C_nO_2$ multilayer MXenes are roughly twice as large as those predicted for Ti-based monolayer MXenes.[27,28] Increasing the interlayer spacing in multilayer MXenes can alter the mobility of the Li atom and significantly improve their adsorption capability. Our study has a high potential to enhance LIBs with different types of cointercalation insertion via DFT studies.

In this work, the monolayer and bilayer of carbide MXenes, the most prevalent type, have been studied. The lightweight of transition metal-based M_2CT_2 (M = Sc, Ti, V, Nb, and Cr; T = O and F) MXenes is investigated as the proposed compound because of their significant theoretical gravimetric capacity.[9,18,19,29] We first explored the energetically favorable structure of the O- and F-functionalized monolayers to construct the bilayer structure. Second, the bilayer structural characteristics (stacking patterns with various sites of the functionalized monolayers) have been investigated to serve as the basis structures for Li diffusion inside the interface. The study of the Li mobility of the oxygen-functionalized MXenes (Ti_2CO_2) is highlighted, which is predicted to have the highest gravimetric capacities of all functionalized MXenes.

2. COMPUTATIONAL DETAILS

The structural properties of the monolayer and bilayer for the M_2CT_2 (M = Sc, Ti, V, Nb, and Cr; T = O and F) MXenes have been obtained using self-consistent DFT simulations with the projector augmented wave method, as implemented in VASP.[30,31] The Perdew−Burke−Ernzerhof (PBE) approach has been employed to handle exchange−correlation energy in the Kohn−Sham equation.[32] Ionic coordinates were relaxed by using the conjugate gradient approach with a 0.01 eV/Å force convergence threshold. The cutoff energy of the plane wave expansion is 500 eV. The Γ-centered Monkhorst−Pack k-mesh of 12 × 12 × 1 has been used for Brillouin zone integrations of the hexagonal-like structure. The van der Waals interactions have been considered within the DFT-D3 method of Grimme with a zero-damping function to appropriately represent weak interactions between layer structures.[33−35] To avoid interactions between the contacting surfaces in the calculations, a vacuum spacing of 20 Å is used.

By calculating the binding energy of the surface functional groups (T = O and F), the computation can predict the preferable site for the T atom adsorbed on the M_2C layer, which may indicate the favorable structure of MXenes.[18] The binding energy of the M_2CT_2 configuration ($E_{\text{bind}}^{M_2CT_2}$) is defined as

$$E_{\text{bind}}^{M_2CT_2} = E^{M_2CT_2} - E^{M_2C} - 2E^{T} \quad (1)$$

According to this definition, the greater negative binding energies indicate the energetic favorability of the T atoms adsorbing on both surface sides of the pristine layer. E^T is the energy of the O or F atom (in this work, we used the total energy of the O_2 or F_2 molecule, which is −0.165 or −0.175 eV per atom, respectively). The exchange−correlation functional of the PBE approach, which is comparable to the MXenes calculations, is used in the calculations for the O_2 or F_2 molecules. A k-mesh of 1 × 1 × 1, energy cutoff for the

https://doi.org/10.1021/acsaem.4c01011
ACS Appl. Energy Mater. XXXX, XXX, XXX−XXX

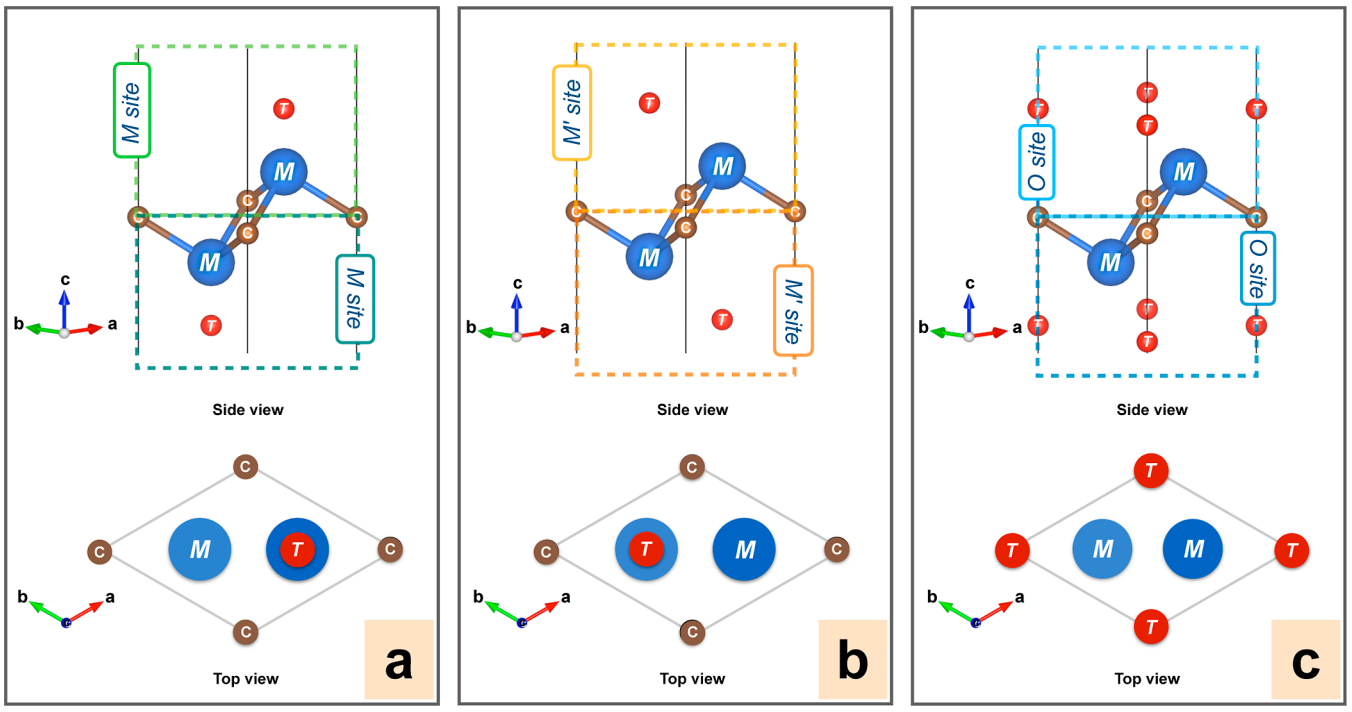

Figure 1. Structural models of the M_2CT_2 monolayer include three possible stacking sites for the surface functional groups, which can be distinguished as (a) *M*-site, (b) *M*′-site, and (c) *O*-site, respectively. Blue, brown, and red indicate the locations of *M* (*M* = Sc, Ti, V, Nb, and Cr), C, and *T* (*T* = O and F), respectively. For the surface functional groups (*M*, *M*′, and *O*-sites), the dashed rectangles outline the repeated cell for various combination types.

plane-wave basis set of 400 eV, and nonspin polarization are used in the calculations for the box size of 20 × 20 × 20 Å^3. Generally, the energy of the *T* atom depends on the choice of references. Note that the relative stability among configurations of the same compound is not affected by the chemical potentials of O or F.

Energetically favorable monolayer configurations for subsequent bilayer investigations have been identified. An extensive set of surface-type combinations (*M*, *M*′, and *O*) for the monolayer has been extensively investigated (Figure 1). Bilayer structures play a crucial role in understanding Li atom insertion as the interlayer spacing can be dynamically adjusted through intercalation. The selective dynamics have been used to investigate the diffusion barrier of the Li atom as a function of the interlayer spacing. We employed a 2 × 2 × 1 supercell to prevent interactions between Li atom periodic images and a 6 × 6 × 1 Brillouin zone sampling. Diffusion barriers have been calculated using static potential energy and climbing image-nudged elastic band (CI-NEB) methods.[27,36] To explore the effect of potassium (K) cointercalation on Li diffusion in the bilayer, the selectivity for Li diffusion as a function of temperature is defined as the ratio of the diffusion rate at a given condition to the reference diffusion rate (k_0) at a reference configuration (diffusion barrier E_0 and temperature T_0). In electronic structure measurements, such as angle-resolved photoemission spectroscopy, temperatures typically range from a few Kelvin to several hundred Kelvin. To provide information for experiments, we present the data within a moderate temperature range, including room temperature. One can simply understand how sensitive the selectivity is at low versus high temperatures in this temperature range. For simplicity, 100 K has been chosen as a reference to illustrate how many orders of magnitude change with each incremental temperature change. Thus, the selectivity (S) is given by

$$S = \frac{k_{d,T}}{k_0} = \frac{A e^{-E_b(d)/k_B T}}{A_0 e^{-E_0/k_B T_0}} \quad (2)$$

where $k_{d,T}$ is the diffusion rate of a chosen system with a given *d*-spacing and temperature (T), A is the diffusion prefactor, A_0 is the diffusion prefactor of the reference diffusion rate, k_B is the Boltzmann constant, and E_b is the diffusion barrier. We know that the quantity of the diffusion prefactor is constant for every simulation, but we do not know the exact values for a particular system. Thus, the diffusion prefactor (A/A_0) ratio would be simplified by arbitrarily defining it as equal to 1. If the prefactor is known, the proper results exhibit a linear scaling of the calculated values.

3. RESULTS AND DISCUSSION

3.1. Structural and Electronic Properties. The multilayer structure of the M_2C MXenes is normally combined with a hexagonal close-packed stacking that corresponds to the hexagonal building blocks of their precursors, as shown in Figure 1.[6,7,15,19,26] The C atoms are located inside the tightly packed structure of the *M* atoms, performing the octahedral interstitial sites. The location of the *T*-functionalized atoms on the M_2C surface is labeled as *M*, *M*′, and *O* surface types in Figure 1. The *M*, *M*′, and *O* sites for the *T* atoms are vertically located above the *M*, *M* with the opposite site, and C atoms, respectively (Figures 1a–c).[7,9,15,19] Different types of surface combinations, symmetric structures (including *MM*, *M*′*M*′, and *OO* models), and asymmetric structures (including *MM*′, *M*′*O*, and *MO* models) are distinguished.[37] For example, the *M*′*O* model is the combination of the rectangle cell, as shown in Figure 1b and c.

https://doi.org/10.1021/acsaem.4c01011
ACS Appl. Energy Mater. XXXX, XXX, XXX−XXX

The calculations of the binding energy for the M_2CO_2 and M_2CF_2 monolayers are presented in Figure 2. Interestingly, the

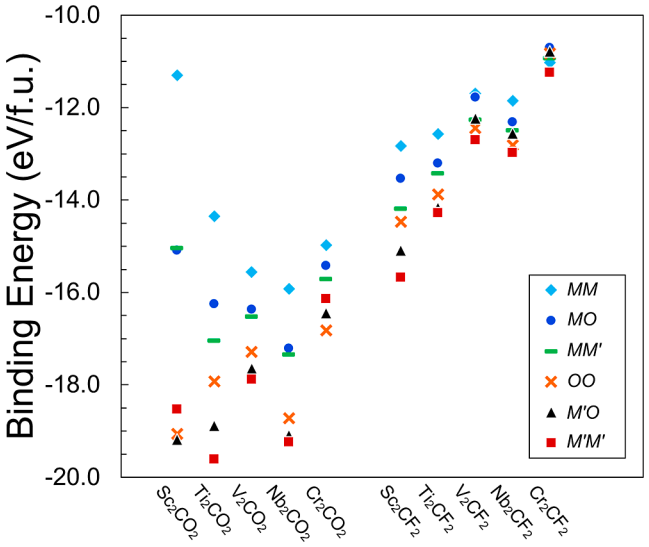

Figure 2. Binding energy for the M_2CO_2 and M_2CF_2 (M = Sc, Ti, V, Nb, and Cr) monolayers consisting of the $M'M'$, $M'O$, OO, MM', MO, and MM models.

$M'M'$, $M'O$, and OO models constitute a set of the M_2CT_2's favorable models. Since the symmetry and stability of a series of M_2CT_2 compounds are the main objectives of this work, nonspin-polarized calculations have been carried out. On the other hand, the ferromagnetic (FM) and antiferromagnetic (AM) ground states for V_2CT_2[38] and Cr_2CT_2[39] have been reported in specific circumstances, depending on the method used.[19] This would raise the degree of freedom to consider the bilayer configurations regarding Hubbard-U parameters apart from surface type, interfacing (e.g., FM/FM, FM/AM, and AM/AM interfaces), and stacking. This theoretical consideration may be devoted to further study. Most structural models have identical patterns consisting of favorable structures ranked by the $M'M'$, $M'O$, OO, MM', MO, and MM models. Therefore, the ranking of surface-type combinations, from most to least favorable, corresponds to M', O, and M. The V_2CF_2, Nb_2CF_2, and Cr_2CF_2 exhibit similar trends with a small difference (SD) in the binding energies (a compound with a narrower energy range between the highest and lowest energy). For applications, compounds with a large difference (LD) in the binding energies have a higher tendency to obtain a specific model compared to compounds that of the SD compound. However, the SD compound has a high chance of obtaining phase mixing between the structural models. In turn, this mixing might be beneficial for a wider range of working conditions.

The larger size of the transition metal may contribute to the narrower energy range between the highest and the lowest. We also plotted the density of state (DOS) using the Sumo command-line tool to explore the association between the functional groups' adsorption locations. Figure 3 shows an example of the DOS for the Ti_2CO_2 monolayer.[40] The Ti-d and O-p states near the valence band edge experience a slight shift toward the lower energy zone, resulting in a reduction of binding energy. The calculated DOS of other compounds is illustrated in Figures S1−S9. We concluded that the energetically favorable model of the monolayer M_2CT_2 correlates to the DOS occurring in the low-energy region (primarily evidenced by the $M'M'$ models). The studied compounds prefer the $M'M'$, $M'O$, and OO models, so we will promote the combination of these models for bilayer structures. The following section examines possible combinations, interfaces, and stackings (rotation and translation) among the three models.

3.2. Selection of the Most Stable Configuration. It has been shown that most of the studied compounds prefer the $M'M'$, $M'O$, and OO models; therefore, combinations of these models are further investigated for bilayer structures. A set of possible combinations, interfaces, and stackings (translation and rotation, as shown in Figure 4) among the three models has been considered. The calculated binding energies of 600 distinct structures are presented in Figure 5. It has been found that the $M'M'$−$M'M'$ with s_6 configurations are energetically favorable among all the compounds, except for the Sc_2CO_2 and Cr_2CO_2 compounds that prefer the OM'−$M'O$ and OO−OO bilayers (with s_4 configurations), respectively. The bilayer's

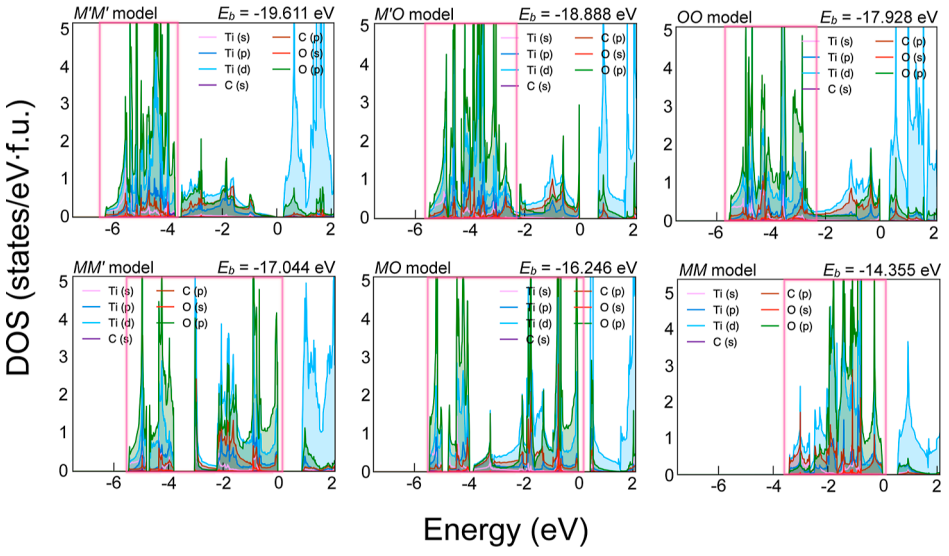

Figure 3. PDOS of Ti_2CO_2 with the $M'M'$, $M'O$, OO, MM', MO, and MM models.

https://doi.org/10.1021/acsaem.4c01011
ACS Appl. Energy Mater. XXXX, XXX, XXX−XXX

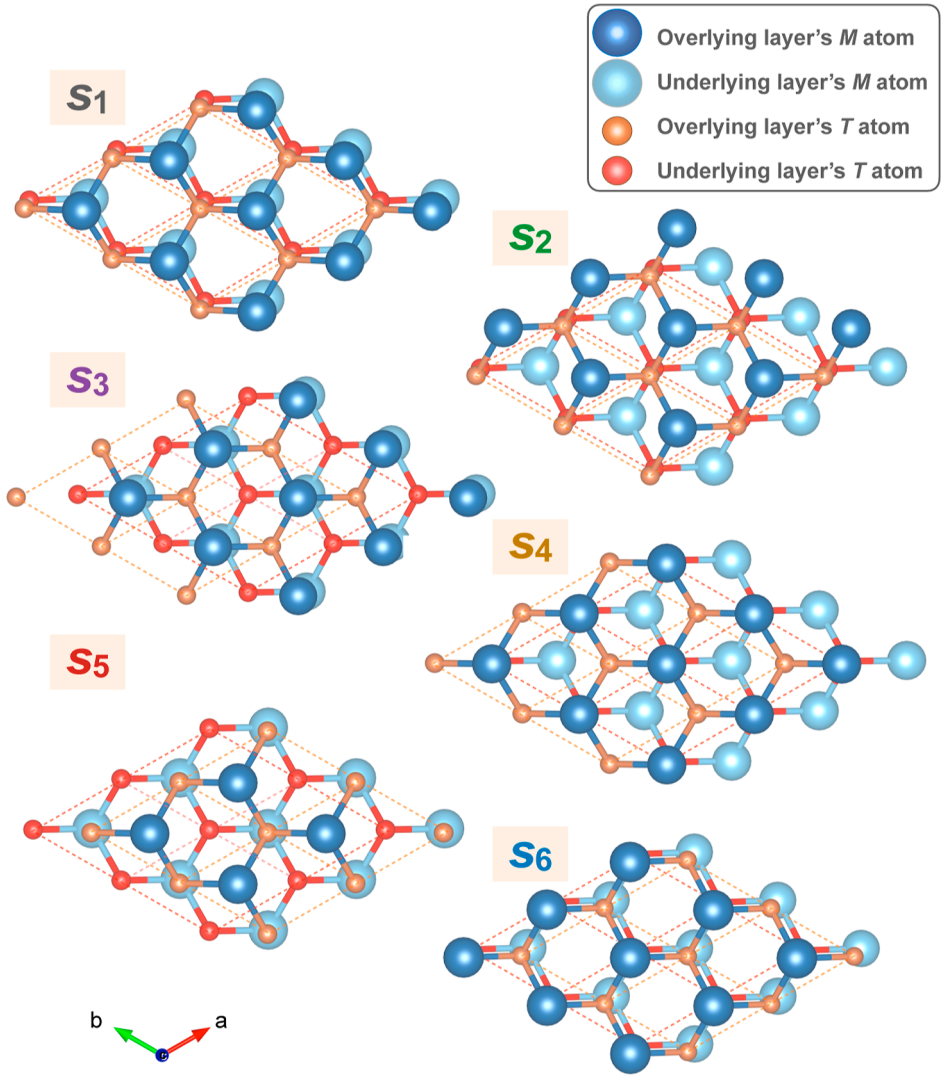

Figure 4. Illustration of the stacking configurations includes the s_1, s_2, s_3, s_4, s_5, and s_6 configurations where M = Sc, Ti, V, Nb, and Cr; T = O and F. The side views of atomic structures for all bilayers are provided in Supporting Information Figure S10.

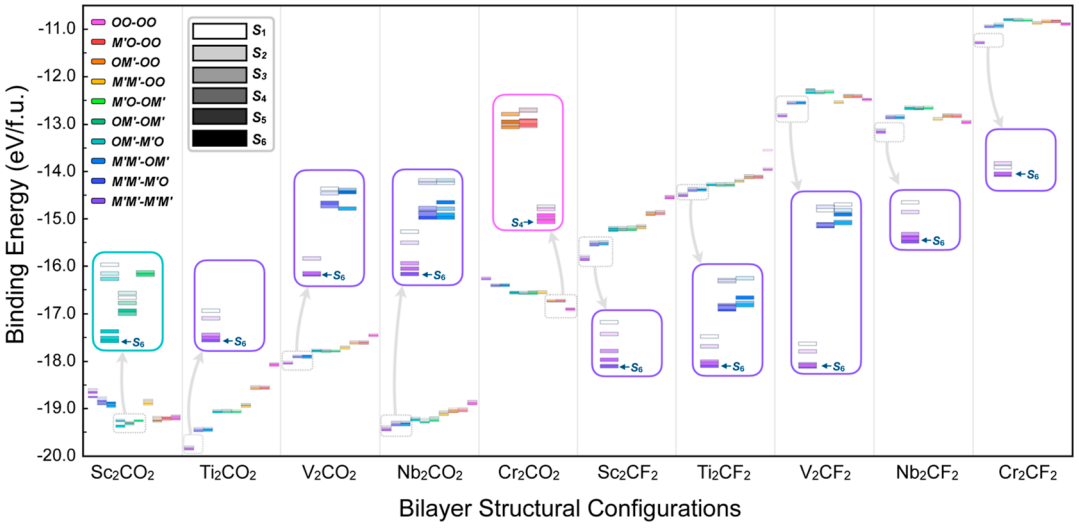

Figure 5. Binding energy of the M_2CT_2 where M = Sc, Ti, V, Nb, and Cr; T = O and F. The various bilayer combinations are categorized according to the color schemes in the inset. The color intensity indicates the stacking s_1, s_2, s_3, s_4, s_5, and s_6 configurations in Figure 4.

https://doi.org/10.1021/acsaem.4c01011
ACS Appl. Energy Mater. XXXX, XXX, XXX−XXX

combination type, stacking configuration, and binding energy of the energetically favorable structures are summarized in Table S1. When all of the combination types of M_2CT_2 bilayers are compared, the binding energy characteristics of the stacking configurations tend to follow an identical pattern, showing that they are slightly altered as the configuration changes. For example, the s_6 configuration mainly emerges as the majority configuration. Interestingly, the second most preferred configuration is the s_5, which corresponds to the rotation of $\pi/3$ radians for the bilayer's overlying layer of the s_6. The shift in binding energy caused by a different type of bilayer combination in the same molecule is greater than the shift caused by the transformation of the stacking configuration. Therefore, altering the bilayer's combination type instead of stacking configurations has a more significant impact on the binding energy of functionalized atoms. The $M'M'-M'M'$ with the s_6 configuration has been shown to be the most energetically favorable structure among all the compounds. This type of structure will be used in the next section to examine the characteristics of Li atom diffusion and their dependence on the interlayer spacing.

3.3. Diffusion Properties and Dependence on Interlayer Spacing. From the previous section, it has been found that the $M'M'-M'M'$ with the s_6 configuration is the most energetically favorable structure among all the compounds. This section considers the framework for Li diffusion properties in bilayer MXenes by using Ti_2CO_2 as a case study. The energetically favorable adsorption location for the Li atom in the Ti_2CO_2 bilayer is identified as the initial state (IS) for Li adsorption. In Figure 6a, the two high-symmetry diffusion paths for the bilayer have been shown. The diffusion Path I is Li migration from the initial site (initial state) to an adjacent site through the hollow channel. The diffusion Path II is the migration from the same initial site to the location between Ti and O atoms. The transition states (TS) of the diffusion paths for Path I and Path II are investigated by CI-NEB methods and indicated as TS-I and TS-II, respectively. The computed diffusion barriers from the CI-NEB methods are 0.78 and 0.36 eV at the TS-I and TS-II, respectively, as shown in Figure 6b. Surprisingly, the relaxation of Li along the c-axis significantly decreases the diffusion barrier for Path II, which is different from the barrier of 0.63 eV obtained by considering Li at the halfway point between two MXenes layers by Ashton et al.[27] Our findings reveal that the Li−O bonding adopts a tetrahedral form for TS-II (Figure 6a) and has a lower diffusion barrier than the octahedral form for TS-I (Figure 6a). The DOS plots in Figure S11 reveal similar characteristics for the Li atoms at TS-I and TS-II, indicating weak interactions with neighboring atoms. The difference in the diffusion barrier primarily arises from structural distortions surrounding the Li atom. The distances between the Li atom and its neighboring atoms at TS-I and TS-II, as illustrated in Figure 6a, are summarized in Table S2.

Furthermore, the relative energy and diffusion barrier as a function of varying interlayer spacing (d-spacing) have been investigated using the inexpensive static potential energy surface (SPES) method for TS-I and TS-II derived from CI-NEB. This study aims to see how the diffusion barriers of the Li atom in bilayer MXenes alter as the d-spacing increases. In practice, the interlayer is fixed in the direction of the c-axis by anchoring two of the Ti atoms in the z-coordinates (the anchoring atoms are indicated by dashed circles in Figure 6a) to specify the interlayer spacing during structural relaxation

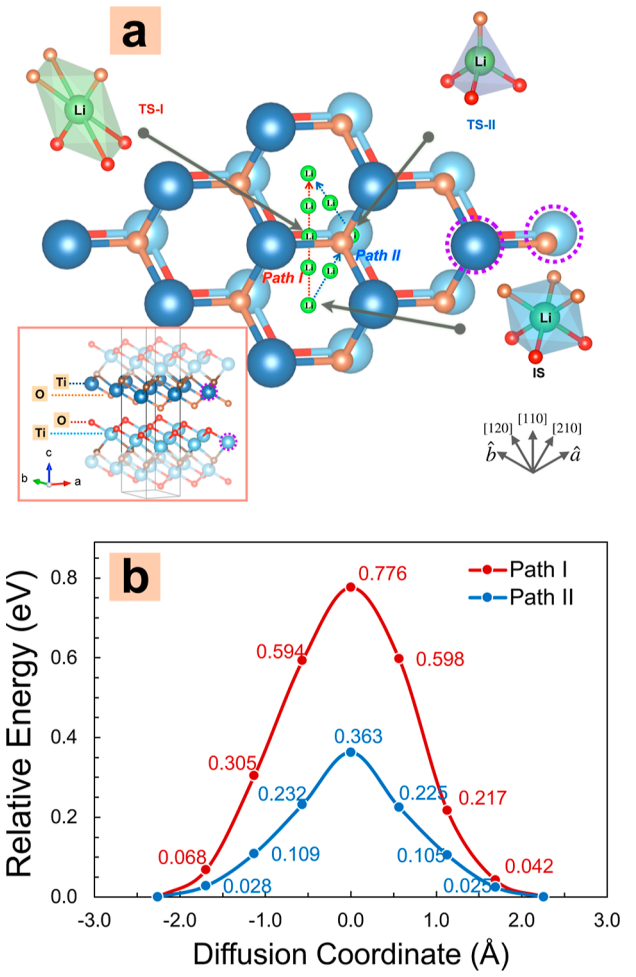

Figure 6. (a) Ti and O layer at the $M'M'-M'M'$ with the s_6 configuration (see the text) interface of Ti_2CO_2, where two of the Ti atoms are anchored in the z-coordinates (the anchoring atoms are indicated by dashed circles). The diffusion paths are partitioned into two high-symmetry routes: diffusion path I and path II, (b) computed diffusion barriers with the CI-NEB methods at the TS-I (red line) and TS-II (blue line) of the Li atom diffusion.

calculations. The average distance along the c-axis (the [001] direction) between the oxygen atoms of the overlaying and underlying layers, which are far from or do not interact with the Li atom at the interface, was used to determine the value of the d-spacing. The plot of relative energy (reference to the IS of the Li atom at equilibrium d-spacing) for both diffusion paths is shown in Figure 7a. The data set shown is the actual d-spacing after relaxation calculations (the d-spacings for IS, TS-I, and TS-II were set to the same value before relaxation by using selective dynamics in the VASP package). The slight shift among the three compounds indicates how the structure relaxes according to the position of Li. The equilibrium d-spacing of IS, TS-I, and TS-II is 2.74, 3.27, and 3.14 Å, respectively. The diffusion barriers for Li's diffusion paths I and II would be 0.44 and 0.35 eV, respectively. Since the time response of lithium mobility is greater than that of the lattice relaxation between the two layers, we propose that the diffusion barrier is reliably obtained by the difference in energy between the transition state (TS-I or TS-II) and the IS at the same d-spacing, as shown in Figure 7b. Therefore, the diffusion barriers for the TS-I and TS-II sites were 1.02 and 0.68 eV, respectively (corresponding to d-spacing of 2.74 Å from Li's

https://doi.org/10.1021/acsaem.4c01011
ACS Appl. Energy Mater. XXXX, XXX, XXX−XXX

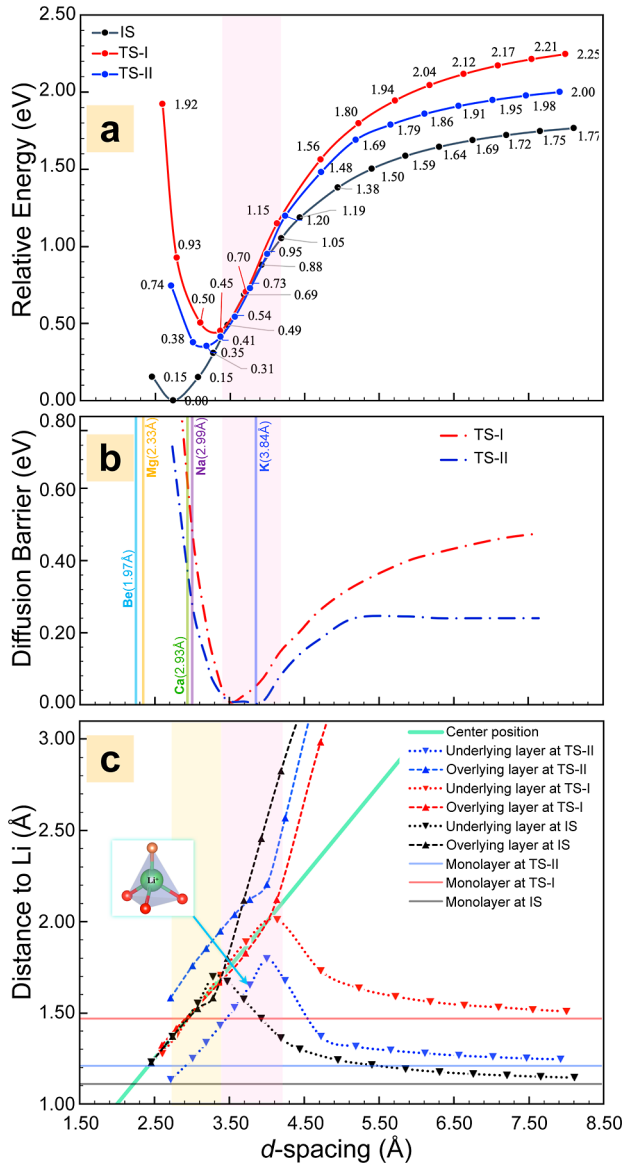

Figure 7. (a) Relative energy for both the TS-I and TS-II (see the texts), (b) diffusion barrier for the TS-I and TS-II [calculated by using the relative energy between the IS and TS-I sites (or TS-II site) for varying *d*-spacings], and (c) distance to Li (in the *c*-axis) from the overlying and underlying layers of the bilayer and monolayer for the IS (black), TS-I (red), and TS-II (blue) as a function of *d*-spacing.

equilibrium site at IS). Note that the barriers are slightly higher than the calculated values by the CI-NEB calculations (0.78 and 0.36 eV). It is interesting to note that the energy at the IS, TS-I, and TS-II of the Li-transition sites exhibits similar ascending features and obviously overlaps with each other in the *d*-spacing range between 3.4 and 4.1 Å (shaded area is given in Figure 7a), indicating an ultralow diffusion barrier in this region (shaded area is given in Figure 7b). The diffusion barrier achieves the lowest value at the *d*-spacing of around 3.5 Å for both TS-I and TS-II. The diffusion barrier of the TS-II increases and approaches the value of 0.24 eV at the *d*-spacing around 5 Å, comparable to the value of 0.22 eV in the case of Li migration on the equivalent site in the monolayer. This indicates that the bilayer with a *d*-spacing larger than this limit is approximately considered as two separated monolayers. Beyond this limit, such as in the cointercalation of solvent molecules, significant irreversible structural changes occur, thereby contributing to the onset of performance degradation.[41]

It is interesting to investigate the distance on the *c*-axis between the Li atom and both layers for IS, TS-I, and TS-II, as shown in Figure 7c. The green slope line depicts the center position (half of the *d*-spacing) between the overlying and underlying layers, which increases as the *d*-spacing rises. The horizontal lines represent the distance between the Li atom and the monolayers for three Li-adsorption sites that correspond with IS, TS-I, and TS-II (gray, red, and blue lines, respectively). The ultralow diffusion barrier is explained by examining the center position of the Li atom between the bilayers. The Li atom at IS, residing at the center of the overlaying and underlying layers up to the *d*-spacing around 3.4 Å, makes it obvious that the Li atom prefers to interact with both layers equally. At larger *d*-spacing, the Li atom tends to interact with one layer more than another, either the overlying or the underlying layer (the underlying layer in this case). The Li atom at the TS-I site tends to interact with the adjacent layer (underlying layer) at a *d*-spacing of 4.2 Å. In contrast, the TS-II site occurs at a *d*-spacing of 4 Å. Consequently, the ultralow diffusion barrier is achieved at the *d*-spacing of around 3.4 to 4.1 Å, and Li atom can migrate in both TS-I and TS-II channels. The findings highlight the significance of the tunability of Li diffusion. The cointercalations can be utilized to vary the interlayer spacing. The interlayer spacings of intercalated Ti_2CO_2 with selected elements, i.e., Be, Mg, Ca, Na, and K, are shown in Figure 7b. The K intercalated Ti_2CO_2 has an interlayer spacing of 3.84 Å, which incidentally falls into the ultralow diffusion barrier range (3.4−4.1 Å). The K intercalation is the prime candidate for further investigation of cointercalations.

3.4. Tuning Layer Spacing and Enhancing Diffusion: The Impact of K Cointercalation. The inclusion of cointercalated elements such as Ca, Na, and K in Ti_2CO_2 is significant for altering the interlayer spacing. The results in Figure 7b suggest that K-intercalated Ti_2CO_2 leads to an ultralow diffusion barrier for Li atoms. In this section, the cointercalation atoms are simulated by fully doping K into the interlayer of the $M'M'-M'M'$ structure of the Ti_2CO_2, approximately 10% doping (one atom in the unit cell). In the cointercalations, the important question is how the K atom affects the diffusion of Li. Here, we consider the relative diffusion rate or selectivity of Li with respect to K. The diffusion barrier of K in the bilayers was considered similar to that of Li. The calculated diffusion barrier of the K atom at TS-I and TS-II is 0.550 and 0.542 eV, respectively. The lower value of 0.542 eV has been used for further calculation. Using eq 2, the general features of the ionic relative diffusion rate in the materials might be primarily obtained. The reference diffusion rate (k_0) is the diffusion rate of Li along Path II with a *d*-spacing of 2.74 Å, an energy barrier of 0.74 eV (the diffusion barrier of Path II), and a temperature of 100 K. The calculated diffusion barrier from Figure 7b and the selectivity (using Path II) of the Li atom at temperatures of 100, 200, 300, and 400 K are shown in Figure 8. The selectivity is shown to be significantly enhanced up to approximately 36 orders of magnitude compared with reference k_0. The maximum selectivity has unnoticeable change and exhibits temperature independence due to the ultralow diffusion barrier around 3.4−4.1 Å, allowing it to be used even at very low temperatures while preserving excellent performance for the diffusion

https://doi.org/10.1021/acsaem.4c01011
ACS Appl. Energy Mater. XXXX, XXX, XXX−XXX

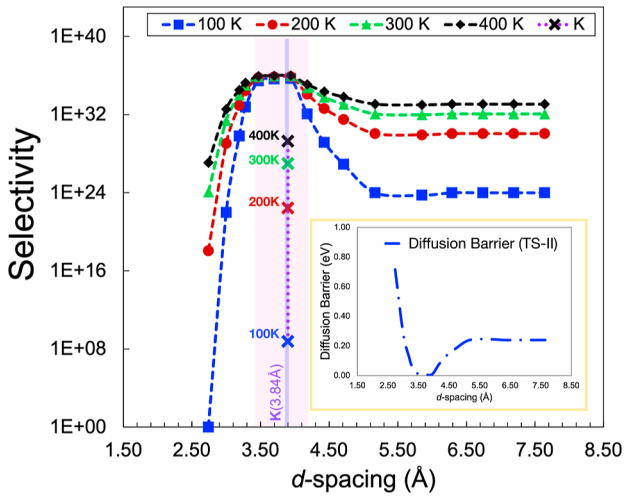

Figure 8. Selectivity (using the Li diffusion barrier at the TS-II) of the Li atom at a chosen temperature, including 100, 200, 300, and 400 K, and the selectivity of the K cointercalations.

characteristics. At larger *d*-spacing, the selectivity decreases (due to the Li atom's tendency to interact with one layer more than another). It reaches a saturated value when the *d*-spacing is above 5.5 Å (approximately the limit to consider a bilayer as two separated monolayers), where the selectivity is obtained by 24, 30, 32, and 33 orders of magnitude for the temperatures of 100, 200, 300, and 400 K, respectively.

The diffusion rate (and selectivity) of the Li atom ranges from 6 (at 400 K) to 25 (at 100 K), orders of magnitude higher than that of the cointercalation atom, K, indicating an extremely high selectivity for Li in the presence of K. As a result, the Li selectivity is much higher than that of the K atom, so the K diffusion does not interfere with the Li. As the temperature rises, the selectivity of K increases faster than that of the Li. For a room temperature of 300 K, our findings show that the selectivity of the Li is approximately 10^8 times higher than the selectivity of the K. For battery applications, K has the potential to be an excellent cointercalation atom because, during the deintercalation process, the expander (which is K in this case) shows a lower diffusion rate than that of the Li in the Ti_2CO_2 bilayer. This means that the K atom can maintain the interlayer spacing of the bilayer to keep the ultralow diffusion barrier for the Li and stabilize the volume of the bilayer.

4. CONCLUSIONS

The framework for the LIB study of the Ti_2CO_2 bilayer with the s_6 stacking configuration (Figure 4) of the $M'M'-M'M'$ bilayer's combination type is explored. We used the CI-NEB and SPES methods to simulate the diffusion barrier for diffusion paths I and II. As a result, the computed diffusion barrier for the CI-NEB methods is 0.78 and 0.36 eV for diffusion paths I and II, respectively. The SPES approach is subsequently used to simulate the trend of the diffusion barrier for those two transition parts as a function of the interlayer spacing (*d*-spacing). We discovered that interlayer spacings ranging from 3.4 to 4.1 Å allow us to achieve ultralow diffusion barrier characteristics (0.01 eV) for the Li diffusion. As a result, it is assumed that the Li atom is neglected by both Ti_2CO_2 layers at the bilayer interface when the interlayer distance is appropriate. Interestingly, the K cointercalation offers the opportunity to alter the Ti_2CO_2 bilayer's interlayer spacing to about 3.8−4.1 Å, covering the ultralow diffusion barrier characteristic and maintaining its position during Li diffusion. We suggested that the K cointercalation could enhance the LIB's performance (charging rate and volume stabilization) with the Ti_2CO_2 electrodes.

■ ASSOCIATED CONTENT

Supporting Information

The Supporting Information is available free of charge at https://pubs.acs.org/doi/10.1021/acsaem.4c01011.

Side views of atomic structures for bilayer stacking configurations and additional calculated results (PDF)

■ AUTHOR INFORMATION

Corresponding Author

Sirichok Jungthawan − *School of Physics, Institute of Science, Suranaree University of Technology, Nakhon Ratchasima 30000, Thailand; Thailand Center of Excellence in Physics, Ministry of Higher Education, Science, Research and Innovation, Bangkok 10400, Thailand; Center of Excellence in Advanced Functional Materials, Suranaree University of Technology, Nakhon Ratchasima 30000, Thailand;* orcid.org/0000-0003-0989-6512; Email: sirichok@g.sut.ac.th

Authors

Tanawat Sawasdee − *School of Physics, Institute of Science, Suranaree University of Technology, Nakhon Ratchasima 30000, Thailand; Thailand Center of Excellence in Physics, Ministry of Higher Education, Science, Research and Innovation, Bangkok 10400, Thailand*

Thanundon Kongnok − *School of Physics, Institute of Science, Suranaree University of Technology, Nakhon Ratchasima 30000, Thailand; Thailand Center of Excellence in Physics, Ministry of Higher Education, Science, Research and Innovation, Bangkok 10400, Thailand*

Ittipon Fongkaew − *School of Physics, Institute of Science, Suranaree University of Technology, Nakhon Ratchasima 30000, Thailand; Thailand Center of Excellence in Physics, Ministry of Higher Education, Science, Research and Innovation, Bangkok 10400, Thailand; Center of Excellence in Advanced Functional Materials, Suranaree University of Technology, Nakhon Ratchasima 30000, Thailand*

Suwit Suthirakun − *Center of Excellence in Advanced Functional Materials and School of Chemistry, Institute of Science, Suranaree University of Technology, Nakhon Ratchasima 30000, Thailand;* orcid.org/0000-0002-6590-6343

Adisak Boonchun − *Thailand Center of Excellence in Physics, Ministry of Higher Education, Science, Research and Innovation, Bangkok 10400, Thailand; Department of Physics, Faculty of Science, Kasetsart University, Bangkok 10900, Thailand;* orcid.org/0000-0001-6527-4537

Pakpoom Reunchan − *Thailand Center of Excellence in Physics, Ministry of Higher Education, Science, Research and Innovation, Bangkok 10400, Thailand; Department of Physics, Faculty of Science, Kasetsart University, Bangkok 10900, Thailand*

Narasak Pandech − *Thailand Center of Excellence in Physics, Ministry of Higher Education, Science, Research and Innovation, Bangkok 10400, Thailand; Department of Applied Physics, Faculty of Sciences and Liberal Arts,*

https://doi.org/10.1021/acsaem.4c01011
ACS Appl. Energy Mater. XXXX, XXX, XXX−XXX

Rajamangala University of Technology Isan, Nakhon Ratchasima 30000, Thailand

Jariyanee Prasongkit − *Thailand Center of Excellence in Physics, Ministry of Higher Education, Science, Research and Innovation, Bangkok 10400, Thailand; Division of Physics, Faculty of Science, Nakhon Phanom University, Nakhon Phanom 48000, Thailand;* orcid.org/0000-0002-4538-2706

Complete contact information is available at: https://pubs.acs.org/10.1021/acsaem.4c01011

Notes

The authors declare no competing financial interest.

■ ACKNOWLEDGMENTS

This work was supported by (i) Suranaree University of Technology (SUT), (ii) Thailand Science Research and Innovation (TSRI), and (iii) National Science, Research, and Innovation Fund (NSRF) (NRIIS Project Number 195579). S.J. has received funding support from the NSRF via the Program Management Unit for Human Resources & Institutional Development, Research and Innovation (grant number B39G670018). The authors are grateful to Prof. W. Meevasana for a decade of fruitful discussions on potassium intercalation in celebration of the work on quasi-freestanding MoS_2 (*Nano Lett.* **2014**, 14, 1312−1316).

■ REFERENCES

(1) Yoo, E.; Kim, J.; Hosono, E.; Zhou, H.-s.; Kudo, T.; Honma, I. Large Reversible Li Storage of Graphene Nanosheet Families for Use in Rechargeable Lithium Ion Batteries. *Nano Lett.* **2008**, *8* (8), 2277−2282.

(2) Jing, Y.; Zhou, Z.; Cabrera, C. R.; Chen, Z. Metallic VS_2Monolayer: A Promising 2D Anode Material for Lithium Ion Batteries. *J. Phys. Chem. C* **2013**, *117* (48), 25409−25413.

(3) Naguib, M.; Kurtoglu, M.; Presser, V.; Lu, J.; Niu, J.; Heon, M.; Hultman, L.; Gogotsi, Y.; Barsoum, M. W. Two-Dimensional Nanocrystals Produced by Exfoliation of Ti_3AlC_2. *Adv. Mater.* **2011**, *23* (37), 4248−4253.

(4) Mashtalir, O.; Naguib, M.; Mochalin, V. N.; Dall'Agnese, Y.; Heon, M.; Barsoum, M. W.; Gogotsi, Y. Intercalation and delamination of layered carbides and carbonitrides. *Nat. Commun.* **2013**, *4* (1), 1716.

(5) Naguib, M.; Come, J.; Dyatkin, B.; Presser, V.; Taberna, P.-L.; Simon, P.; Barsoum, M. W.; Gogotsi, Y. MXene: a promising transition metal carbide anode for lithium-ion batteries. *Electrochem. Commun.* **2012**, *16* (1), 61−64.

(6) Naguib, M.; Mashtalir, O.; Carle, J.; Presser, V.; Lu, J.; Hultman, L.; Gogotsi, Y.; Barsoum, M. W. Two-Dimensional Transition Metal Carbides. *ACS Nano* **2012**, *6* (2), 1322−1331.

(7) Khazaei, M.; Arai, M.; Sasaki, T.; Chung, C.-Y.; Venkataramanan, N. S.; Estili, M.; Sakka, Y.; Kawazoe, Y. Novel Electronic and Magnetic Properties of Two-Dimensional Transition Metal Carbides and Nitrides. *Adv. Funct. Mater.* **2013**, *23* (17), 2185−2192.

(8) Naguib, M.; Halim, J.; Lu, J.; Cook, K. M.; Hultman, L.; Gogotsi, Y.; Barsoum, M. W. New Two-Dimensional Niobium and Vanadium Carbides as Promising Materials for Li-Ion Batteries. *J. Am. Chem. Soc.* **2013**, *135* (43), 15966−15969.

(9) Khazaei, M.; Arai, M.; Sasaki, T.; Estili, M.; Sakka, Y. Two-dimensional molybdenum carbides: potential thermoelectric materials of the MXene family. *Phys. Chem. Chem. Phys.* **2014**, *16* (17), 7841−7849.

(10) Naguib, M.; Mochalin, V. N.; Barsoum, M. W.; Gogotsi, Y. 25th Anniversary Article: MXenes: A New Family of Two-Dimensional Materials. *Adv. Mater.* **2014**, *26* (7), 992−1005.

(11) Ghidiu, M.; Naguib, M.; Shi, C.; Mashtalir, O.; Pan, L. M.; Zhang, B.; Yang, J.; Gogotsi, Y.; Billinge, S. J. L.; Barsoum, M. W. Synthesis and characterization of two-dimensional Nb_4C_3 (MXene). *Chem. Commun.* **2014**, *50* (67), 9517−9520.

(12) Srivastava, P.; Mishra, A.; Mizuseki, H.; Lee, K.-R.; Singh, A. K. Mechanistic Insight into the Chemical Exfoliation and Functionalization of Ti_3C_2MXene. *ACS Appl. Mater. Interfaces* **2016**, *8* (36), 24256−24264.

(13) Lashgari, H.; Abolhassani, M. R.; Boochani, A.; Elahi, S. M.; Khodadadi, J. Electronic and optical properties of 2D graphene-like compounds titanium carbides and nitrides: DFT calculations. *Solid State Commun.* **2014**, *195*, 61−69.

(14) Zhao, P.; Desai, S.; Tosun, M.; Roy, T.; Fang, H.; Sachid, A.; Amani, M.; Hu, C.; Javey, A. 2D layered materials: From materials properties to device applications. In *2015 IEEE International Electron Devices Meeting (IEDM)*, 2015; IEEE, pp 27.3.1−27.3.4.

(15) Anasori, B.; Lukatskaya, M. R.; Gogotsi, Y. 2D metal carbides and nitrides (MXenes) for energy storage. *Nat. Rev. Mater.* **2017**, *2* (2), 16098.

(16) Peng, J.; Chen, X.; Ong, W.-J.; Zhao, X.; Li, N. Surface and Heterointerface Engineering of 2D MXenes and Their Nanocomposites: Insights into Electro- and Photocatalysis. *Chem* **2019**, *5* (1), 18−50.

(17) Sun, S.; Liao, C.; Hafez, A. M.; Zhu, H.; Wu, S. Two-dimensional MXenes for energy storage. *Chem. Eng. J.* **2018**, *338*, 27−45.

(18) Fu, Z.; Wang, N.; Legut, D.; Si, C.; Zhang, Q.; Du, S.; Germann, T. C.; Francisco, J. S.; Zhang, R. Rational Design of Flexible Two-Dimensional MXenes with Multiple Functionalities. *Chem. Rev.* **2019**, *119* (23), 11980−12031.

(19) Khazaei, M.; Ranjbar, A.; Arai, M.; Sasaki, T.; Yunoki, S. Electronic properties and applications of MXenes: a theoretical review. *J. Mater. Chem. C* **2017**, *5* (10), 2488−2503.

(20) Eames, C.; Islam, M. S. Ion Intercalation into Two-Dimensional Transition-Metal Carbides: Global Screening for New High-Capacity Battery Materials. *J. Am. Chem. Soc.* **2014**, *136* (46), 16270−16276.

(21) Jindata, W.; Hantanasirisakul, K.; Eknapakul, T.; Denlinger, J. D.; Sangphet, S.; Chaiyachad, S.; Jaisuk, C.; Rasritat, A.; Sawasdee, T.; Nakajima, H.; Rattanachata, A.; Fongkaew, I.; Limpijumnong, S.; Gogotsi, Y.; Meevasana, W. Spectroscopic signature of negative electronic compressibility from the Ti core-level of titanium carbonitride MXene. *Appl. Phys. Rev.* **2021**, *8* (2), 021401.

(22) Zhang, H.; Fu, Z.; Legut, D.; Germann, T.; Zhang, R. Stacking stability and sliding mechanism in weakly bonded 2D transition metal carbides by van der Waals force. *RSC Adv.* **2017**, *7*, 55912−55919.

(23) Luo, J.; Zhang, W.; Yuan, H.; Jin, C.; Zhang, L.; Huang, H.; Liang, C.; Xia, Y.; Zhang, J.; Gan, Y.; Tao, X. Pillared Structure Design of MXene with Ultralarge Interlayer Spacing for High-Performance Lithium-Ion Capacitors. *ACS Nano* **2017**, *11* (3), 2459−2469.

(24) Lukatskaya, M. R.; Mashtalir, O.; Ren, C. E.; Dall'Agnese, Y.; Rozier, P.; Taberna, P. L.; Naguib, M.; Simon, P.; Barsoum, M. W.; Gogotsi, Y. Cation intercalation and high volumetric capacitance of two-dimensional titanium carbide. *Science* **2013**, *341* (6153), 1502−1505.

(25) Xie, Y.; Naguib, M.; Mochalin, V. N.; Barsoum, M. W.; Gogotsi, Y.; Yu, X.; Nam, K.-W.; Yang, X.-Q.; Kolesnikov, A. I.; Kent, P. R. C. Role of Surface Structure on Li-Ion Energy Storage Capacity of Two-Dimensional Transition-Metal Carbides. *J. Am. Chem. Soc.* **2014**, *136* (17), 6385−6394.

(26) Zhang, H.; Fu, Z.; Zhang, R.; Zhang, Q.; Tian, H.; Legut, D.; Germann, T. C.; Guo, Y.; Du, S.; Francisco, J. S. Designing flexible 2D transition metal carbides with strain-controllable lithium storage. *Proc. Natl. Acad. Sci. U.S.A.* **2017**, *114* (52), No. E11082.

(27) Ashton, M.; Hennig, R. G.; Sinnott, S. B. Computational characterization of lightweight multilayer MXene Li-ion battery anodes. *Appl. Phys. Lett.* **2016**, *108* (2), 023901.

(28) Tang, Q.; Zhou, Z.; Shen, P. Are MXenes Promising Anode Materials for Li Ion Batteries? Computational Studies on Electronic Properties and Li Storage Capability of Ti_3C_2 and $Ti_3C_2X_2$ (X = F, OH) Monolayer. *J. Am. Chem. Soc.* **2012**, *134* (40), 16909−16916.
(29) Anasori, B.; Xie, Y.; Beidaghi, M.; Lu, J.; Hosler, B. C.; Hultman, L.; Kent, P. R. C.; Gogotsi, Y.; Barsoum, M. W. Two-Dimensional, Ordered, Double Transition Metals Carbides (MXenes). *ACS Nano* **2015**, *9* (10), 9507−9516.
(30) Blöchl, P. E. Projector augmented-wave method. *Phys. Rev. B* **1994**, *50* (24), 17953−17979.
(31) Kresse, G.; Joubert, D. From ultrasoft pseudopotentials to the projector augmented-wave method. *Phys. Rev. B* **1999**, *59* (3), 1758−1775.
(32) Perdew, J. P.; Burke, K.; Ernzerhof, M. Generalized Gradient Approximation Made Simple. *Phys. Rev. Lett.* **1996**, *77* (18), 3865−3868.
(33) Grimme, S. Semiempirical GGA-type density functional constructed with a long-range dispersion correction. *J. Comput. Chem.* **2006**, *27* (15), 1787−1799.
(34) Yarifard, M.; Davoodi, J.; Rafii-Tabar, H. In-plane thermal conductivity of graphene nanomesh: A molecular dynamics study. *Comput. Mater. Sci.* **2016**, *111*, 247−251.
(35) Grimme, S.; Antony, J.; Ehrlich, S.; Krieg, H. A consistent and accurate ab initio parametrization of density functional dispersion correction (DFT-D) for the 94 elements H-Pu. *J. Chem. Phys.* **2010**, *132* (15), 154104.
(36) Henkelman, G.; Uberuaga, B. P.; Jónsson, H. A climbing image nudged elastic band method for finding saddle points and minimum energy paths. *J. Chem. Phys.* **2000**, *113* (22), 9901−9904.
(37) Guo, J.; Sun, Y.; Liu, B.; Zhang, Q.; Peng, Q. Two-dimensional scandium-based carbides (MXene): Band gap modulation and optical properties. *J. Alloys Compd.* **2017**, *712*, 752−759.
(38) Bae, S.; Kang, Y. G.; Khazaei, M.; Ohno, K.; Kim, Y. H.; Han, M. J.; Chang, K. J.; Raebiger, H. Electronic and magnetic properties of carbide MXenes-the role of electron correlations. *Mater. Today Adv.* **2021**, *9*, 100118.
(39) Si, C.; Zhou, J.; Sun, Z. Half-Metallic Ferromagnetism and Surface Functionalization-Induced Metal-Insulator Transition in Graphene-like Two-Dimensional Cr_2C Crystals. *ACS Appl. Mater. Interfaces* **2015**, *7* (31), 17510−17515.
(40) Ganose, A.; Jackson, A.; Scanlon, D. sumo: Command-line tools for plotting and analysis of periodic ab initio calculations. *J. Open Source Softw.* **2018**, *3*, 717.
(41) Bärmann, P.; Winter, M.; Gonzalez-Julian, J.; Placke, T. Solvent Co-Intercalation-Induced Activation and Capacity Fade Mechanism of Few-/Multi-Layered MXenes in Lithium Ion Batteries. *Small* **2021**, *17* (47), 2104130.

https://doi.org/10.1021/acsaem.4c01011
ACS Appl. Energy Mater. XXXX, XXX, XXX−XXX